

Visual perception and density-sensitive interaction in active agent system

Fei Meng(孟飞), Weiqiang Ma(马维强), Run Cheng(程润), and Jun Wang(王骏)
Citation: Chin. Phys. B, 2026, 35 (**1**): 018702. DOI: 10.1088/1674-1056/adf4a7
http://cpb.iphy.ac.cn; http://iopscience.iop.org/cpb

What follows is a list of articles you may be interested in

Simple robot swarm with magnetic coupling connections can collaboratively accomplish collective tasks

Xingyu Ma(马星宇), Chuyun Wang(汪楚云), Jing Wang(王璟), Huaicheng Chen(陈怀城), Gao Wang(王高), and Liyu Liu(刘雳宇)
Chin. Phys. B, 2025, 34 (**6**): 068701. DOI: 10.1088/1674-1056/adc666

Disorder-to-order transition induced by spontaneous cooling regulation in robotic active matter

Shuaixu Hou(侯帅旭), Gao Wang(王高), Xingyu Ma(马星宇), Chuyun Wang(汪楚云), Peng Wang(王鹏), Huaicheng Chen(陈怀城), Liyu Liu(刘雳宇), and Jing Wang(王璟)
Chin. Phys. B, 2024, 33 (**7**): 078701. DOI: 10.1088/1674-1056/ad4327

Bio-inspired environmental adaptability of swarm active matter

Yangkai Jin(金阳凯), Gao Wang(王高), Daming Yuan(袁大明), Peilong Wang(王培龙), Jing Wang(王璟), Huaicheng Chen(陈怀城), Liyu Liu(刘雳宇), and Xingjie Zan(昝兴杰)
Chin. Phys. B, 2023, 32 (**8**): 088703. DOI: 10.1088/1674-1056/acd688

Orderly hysteresis in field-driven robot swarm active matter

Yanping Liu(刘艳萍), Gao Wang(王高), Peilong Wang(王培龙), Daming Yuan(袁大明), Shuaixu Hou(侯帅旭), Yangkai Jin(金阳凯), Jing Wang(王璟), and Liyu Liu(刘雳宇)
Chin. Phys. B, 2023, 32 (**6**): 068701. DOI: 10.1088/1674-1056/acc803

Discontinuous and continuous transitions of collective behaviors in living systems

Xu Li(李旭), Tingting Xue(薛婷婷), Yu Sun(孙宇), Jingfang Fan(樊京芳), Hui Li(李辉), Maoxin Liu(刘卯鑫), Zhangang Han(韩战钢), Zengru Di(狄增如), and Xiaosong Chen(陈晓松)
Chin. Phys. B, 2021, 30 (**12**): 128703. DOI: 10.1088/1674-1056/ac3c3f

---

Visual perception and density-sensitive interaction in active agent system

Fei Meng(孟飞)[1,†], Weiqiang Ma(马维强)[1], Run Cheng(程润)[2,‡], and Jun Wang(王骏)[1,§]

[1] *National Laboratory of Solid State Microstructure, Collaborative Innovation Center of Advanced Microstructures and School of Physics, Nanjing University, Nanjing* 210093, *China*

[2] *Physics Department of Basic Department, Army Engineering University of PLA, Nanjing* 211101, *China*

(Received 15 May 2025; revised manuscript received 1 July 2025; accepted manuscript online 28 July 2025)

This study extends the self-propelled particle (SPP) model by incorporating a limited vision cone and local density sensing. The results reveal that clusters can simultaneously exhibit velocity polarization and spatial cohesion within specific ranges of vision angle and density threshold. The dependence of the dynamical features, including the order parameter and density variation, on the threshold and visual cone is investigated. Furthermore, a critical threshold is identified, which governs the transition between ordered and disordered states and is closely linked to density fluctuations and noise intensity. The clustering results show that the model is explained by the chasing mechanism responsible for cluster formation, density, and shape. These results may stimulate practical applications in swarm maneuvering.

Keywords: active matter, Vicsek model, visual perception, threshold

PACS: 87.15.Zg, 89.75.Fb, 05.65.+b, 87.85.St

DOI: 10.1088/1674-1056/adf4a7 **CSTR:** 32038.14.CPB.adf4a7

1. Introduction

The phenomenon of collective motion exhibited by active agents across diverse natural and artificial systems has drawn substantial interest, prompting experimental and theoretical investigations. Systems that have been studied include bird flocks,[1] fish schools,[2] bacterial colonies,[3] and human crowds,[4] as well as engineered microswimmer assemblies[5] and robotic/unmanned aerial vehicle (UAV) swarms.[6–12] The local interactions within these systems are understood to give rise to emergent flocking behavior or global order. This phenomenon is well established in the self-propelled particle (SPP) models, wherein each agent tends to align its direction of motion with that of its neighbors within a defined spatial radius.[13] Recent studies have also highlighted the potential influence of heterogeneity at both the individual and environmental levels on collective motion dynamics.[14–17] For example, the SPP model can be extended by introducing a certain proportion of misaligned agents,[15,16] multiple subpopulations,[17] or spatial obstacles.[14,18] The evolution of these systems exhibits complex features such as collective cohesion,[14] self-ordering,[15] and phase separation.[17] In natural systems, heterogeneity within a population may arise from individual differences or spatial position.[19] In a homogeneous flock, changes in the behavioral patterns of certain individuals can induce behavioral shifts in a subset of the flock.

In natural systems, collective organisms dynamically transition between dispersed and cohesive states to adapt to functional needs such as migration or predation.[20–23] These transitions emerge from individual behavioral adjustments guided by local environmental cues, which play a pivotal role in reshaping group-level dynamics.[24–27] For instance, bacterial colonies exhibit density-dependent phase separation by modulating motility through local chemical gradient sensing, as demonstrated experimentally[24] and theoretically.[25,26] Furthermore, recent studies have revealed that switching movement mode based on local alignment degree enables spontaneous phase coexistence and transformation in active matter systems.[27] A notable example is Li *et al.*'s work,[28] where synchronization of collective speed was achieved by coupling individual propulsion speeds to local orientational order. These findings collectively highlight that localized sensing-driven behavioral plasticity serves as a critical mechanism for initiating and regulating macroscopic pattern formation in living aggregates.

In both natural and engineered systems, constrained perception through a limited visual cone is a ubiquitous mechanism used by agents to acquire environmental information.[29–31] Crucially, the introduction of such anisotropic perception breaks the symmetry of Newton's third law, creating nonreciprocal interactions when incorporated into SPP models. These asymmetric social forces profoundly reshape collective dynamics, enabling the emergence of exotic

†Corresponding author. E-mail: 602023220052@smail.nju.edu.cn
‡Corresponding author. E-mail: DG20220011@smail.nju.edu.cn
§Corresponding author. E-mail: wangj@nju.edu.cn

© 2026 Chinese Physical Society and IOP Publishing Ltd. All rights, including for text and data mining, AI training, and similar technologies, are reserved.

macroscopic patterns — including cohesive clusters,[7,32,33] milling vortices,[34,35] and worm-like traveling bands.[35]

In our work, we extend the classical SPP model by incorporating visual perception through a limited vision cone and local density sensing. Specifically, each agent is equipped with a vision cone with an adjustable angular range and a finite sensing radius. Agents dynamically adjust their orientation based on the number of neighbors within their detection zone: if the local density exceeds a predefined threshold, they align with neighbors; otherwise, they maintain their current direction. We demonstrate that this perception-driven mechanism simultaneously generates velocity polarization and spatial cohesion within clusters, provided the vision angle and density threshold fall within specific ranges.

Furthermore, the dependence of the dynamical features, including the order parameter and density variation, on the threshold and vision angle is investigated. Notably, a critical threshold governing the transition between ordered and disordered states is uncovered, which is closely linked to density fluctuations and noise intensity. Finally, the clustering results show that the model is explained by the chasing mechanism responsible for cluster formation, density, and shape. These results may stimulate practical applications in swarm maneuvering.

2. Model and methods

In our work, we consider the incorporation of a perception-response mechanism into the SPP model. That is, the direction of the propelling force is coupled with all the other agents in the perception area (mimicking the SPP model), and the kinetic mode (aligned or unaligned) is determined based on a perception function. Intuitively, the combination of the kinetic features may enable concurrent condensation in both coordinate and momentum spaces.

Agent-based models have received attention in recent years.[36] In our model, we consider N_0 self-propelling agents moving on a two-dimensional square area of linear size L under periodic boundary conditions. An agent perceives a defined spatial region, Ω_i, of its surrounding environment through a perception unit, such as a camera in the case of a robot. The information obtained via perception can be transformed into a perception function, P_i, which determines the motion of agent i. Thus, the agent motion can be described by

$$\theta_i(t+\Delta t) = \theta_i(t) + P_i(t)\left[\Theta\Big(\sum_{j\in\Omega_i}\hat{\boldsymbol{u}}_j(t)\Big) - \theta_i(t)\right] + \sqrt{2D_{\mathrm{R}}\Delta t}\,\xi_i, \tag{1}$$

$$\boldsymbol{r}_i(t+\Delta t) = \boldsymbol{r}_i(t) + V_0\hat{\boldsymbol{u}}_i(t+\Delta t)\Delta t, \tag{2}$$

where $\Delta t = 0.5$ is the time step of the simulation, $\boldsymbol{r}_i$ is the position of the agents, $\hat{\boldsymbol{u}}_i$ is a unit vector indicating the direction of the propelling velocity, V_0 is the size of the propulsion speed, θ_i is the direction angle of $\hat{\boldsymbol{u}}_i$, and $\Theta(\boldsymbol{U})$ is the direction angle of vector $\boldsymbol{U}$. Let θ_i, $\Theta(\boldsymbol{U}) \in [0, 2\pi)$ be the counterclockwise angles from the positive x-axis to $\hat{\boldsymbol{u}}_i$ and $\boldsymbol{U}$. D_{R} is the rotational diffusion constant, and ξ_i is Gaussian noise with zero mean and unit variance. Agents j are in the perception area of agent i. The perception area Ω_i indicates the conical area from the position $\boldsymbol{r}_i$, with a spanning angle of α, a central direction of $\boldsymbol{p}_i = \hat{\boldsymbol{u}}_i(t)$, and a perception radius of R.

The perception function $P_i(t)$ that determines whether agent i aligns with the surrounding agents can be described as follows:

$$P_i(t) = \begin{cases} 1, & \text{if } k_i(t) > P^* \text{ and } \|\sum_{j\in\Omega_i}\hat{\boldsymbol{u}}_j(t)\| \neq 0, \\ 0, & \text{if } k_i(t) \leq P^* \text{ or } \|\sum_{j\in\Omega_i}\hat{\boldsymbol{u}}_j(t)\| = 0, \end{cases} \tag{3}$$

where k_i is the number of agents j within the perception area Ω_i of agent i, and the threshold P^* is a parameter in the model. A schematic diagram is shown in Fig. 1. Our choice of this perception function is inspired by the trade-off between individual conformity and the maintenance of individuality. As P^* increases, individuals retain their direction of motion, whereas a decrease in P^* promotes alignment with neighbors within perceptual range. When $\alpha = 360^\circ$ and $P^* = 0$, our model is similar to the Vicsek model.[13] In the absence of specific declarations, the other parameter settings in the model are set to $N_0 = 10000$, $L = 100$, $V_0 = 0.2$, $R = 2$, and $D_{\mathrm{R}} = 0.01$. The parameter values were primarily selected based on those used in Refs. [7,32]. Indeed, these dynamic rules do not include volume exclusion, making such a setup easier to implement in UAV/robotic systems. In Section 4, we discuss methods for collision avoidance.

The initial state of the system consists of N_0 agents randomly distributed within a square area of side length L, with the directions of the agents being random; the initial density of the system is $\rho_0 = N_0/L^2$. Therefore, the choice of P^* cannot be arbitrary. We can assume that at the initial moment, the agent uses its perception unit to count the number of agents within its perception area, resulting in a value of $P^\alpha = (\alpha/360^\circ)(\rho_0\pi R^2)$. The threshold P^* can be selected based on the value of P^α.

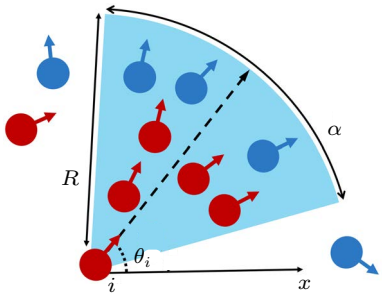


Fig. 1. Schematic diagram of the motion mechanism. α is the perception cone angle of the agent, R is the perception radius, and θ_i is the direction of the propulsion velocity of agent i. The blue agents represent misaligned states, and the red agents represent aligned states.

3. Dynamics of condensation

Based on the kinetic rules indicated by Eqs. (1)–(3), the system of agents should evolve and reach its destination after a sufficient time has elapsed (typically 5×10^4 steps for $N_0 = 10000$). We observed that the agent group exhibits different cohesive shapes depending on the variations in the visual cone angle α and the threshold P^*; several snapshots of the patterns are shown in Fig. 1. All subfigures have the same spatial scales. The black arrows in Fig. 2 indicate the direction of motion of the clusters. It can be observed that under certain α and P^* limits, the group exhibits cohesion, as shown in Figs. 2(b)–2(h). Furthermore, when the visual cone is relatively small ($\alpha \in [20^\circ, 140^\circ]$), nearly all agents aggregate into linear formations, as shown in Figs. 2(b)–2(e). The group forms several clusters, accompanied by a sparse gas state for $\alpha = 360^\circ$, as shown in Fig. 2(h). For intermediate cone angles ($\alpha = 180^\circ$, 230°), the group exhibits a transitional phase marked by the coexistence of linear distribution and clusters, as shown in Figs. 2(f) and 2(g). However, condensation does not necessarily occur. For example, when α is small ($\alpha = 20^\circ$), the threshold is absent (i.e., $P^* = 0$), and the agents remain dispersed, as shown in Fig. 2(a). This seems counterintuitive, as the presence of the threshold P^* reduces the tendency for agents to align with their surrounding agents. Therefore, the control of cluster cohesion by the kinetic rules and the features of the cluster are the main issues to be studied.

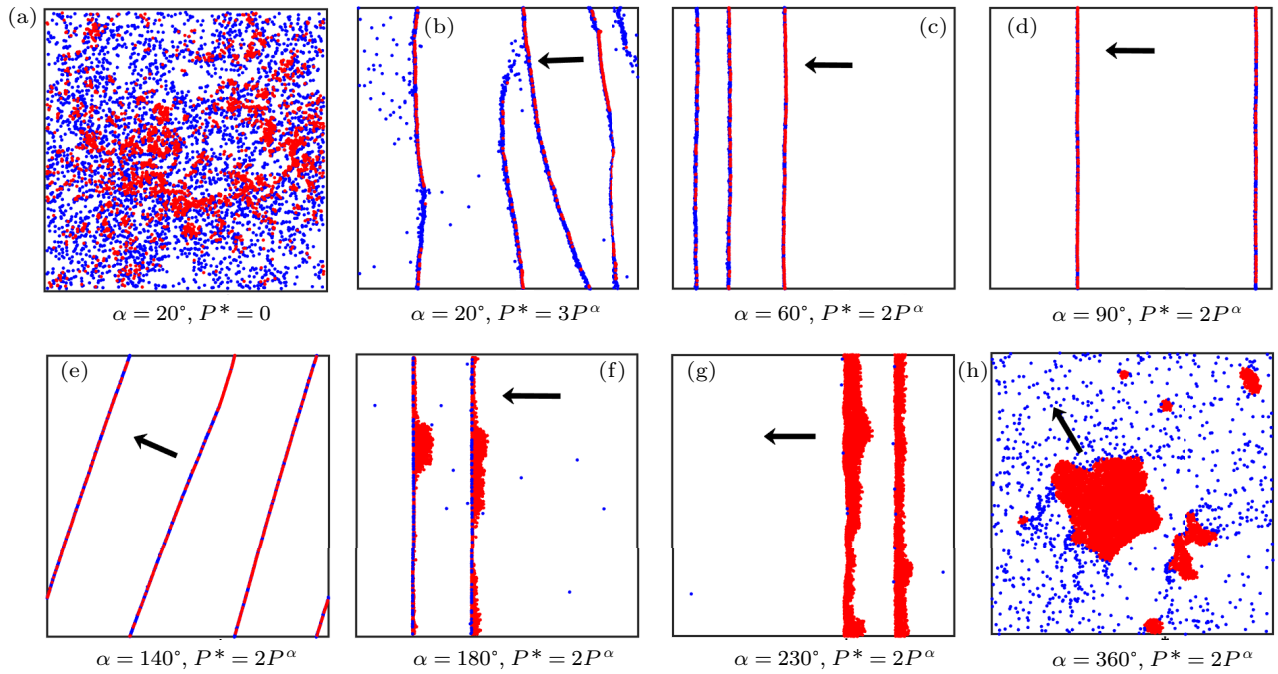


Fig. 2. Typical snapshots of agents with visual cones of $\alpha = 20^\circ$, 60°, 90°, 140°, 180°, 230°, and 360° and varying thresholds P^*. The number of agents is $N_0 = 10000$, $D_R = 0.01$, and the number of steps is 5×10^4. Blue agents represents misaligned states, and red agents represent aligned states. The black arrows indicate the direction of cluster motion.

The simulation results indicate that clusters can maintain spatial cohesion over an extensive range of visual cone ($\alpha \in [20^\circ, 360^\circ]$), although this is influenced by the threshold P^*. The cluster density $\rho = n_c/S$ is used as a measure of spatial cohesion, where n_c is the number of agents in the clusters and S represents the area of the clusters. Agents i and j are considered to belong to the same cluster if their distance is less than R and $\hat{\boldsymbol{u}}_i \cdot \hat{\boldsymbol{u}}_j > 0.5$. To calculate the cluster area, the square simulation domain is discretized into grid cells of unit length (1×1). The cluster area is then determined by counting the number of grid cells occupied by the clusters. It can be observed that the clusters remain cohesive within a threshold range of $P^* \in [P^\alpha, 2.5P^\alpha]$, as shown in Fig. 3(a). The density of clusters within this threshold range is significantly higher than that of clusters without a threshold ($P^* = 0$). Moreover, as P^* increases, the density ρ of the clusters also rises, suggesting that the modulation of motion patterns induced by the threshold enhances the spatial cohesion of the clusters. However, cohesion does not inevitably occur. When P^* is excessively large, the clusters tend to disaggregate. In addition to spatial cohesion, the collective motion of clusters is also observed in Fig. 2. To quantify the velocity condensation, an order parameter $\Psi = |\sum_{i=1}^{N} \boldsymbol{v}_i|/(N_0 V_0)$ is defined. Ψ attains values close to 1 within a threshold range of $P^* \in (0, 2.5P^\alpha]$, implying that clusters condense in velocity space, as shown in Fig. 3(b). Ψ is notably higher in the presence of a threshold compared to the $P^* = 0$ case, indicating enhanced velocity condensation. Ψ remains near one as P^* increases until it abruptly diminishes to zero beyond a critical value (e.g., $2.5P^\alpha$). This sharp transition signifies a loss of velocity coherence and a shift toward a disordered state. As shown in Fig. 3, simultaneous cohesion in both spatial and velocity space is observed within a specific

threshold range, $P^* \in (0, 2.5P^{\alpha}]$. This is understandable, as inconsistent cluster velocities would promote fragmentation, leading to decreased cluster density. This observation suggests that the order parameter Ψ can be used to determine whether cluster cohesion occurs.

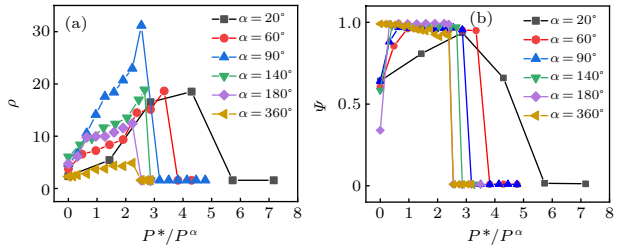


Fig. 3. Cohesion and polarization of clusters with visual cones of $\alpha = 20°$, $60°$, $90°$, $140°$, $180°$, and $360°$. (a) The cluster density ρ as a function of the threshold P^*. (b) The order parameter Ψ as a function of the threshold P^*.

In addition to the influence of the threshold P^* on cluster cohesion, noise is also an important factor affecting the cohesion process. To establish a more comprehensive picture of the formation of the structure, we further calculate the phase diagram for various values of P^* and rotational diffusion D_{R} at different visual cone angles α, as shown in Fig. 4. The order parameter Ψ is used as a measure of cluster cohesion. Red areas visually represent cluster cohesion. It can be observed that compact clusters can only be realized in the lower-left region of the phase diagram, corresponding to low values of both P^* and D_{R}. As D_{R} increases, the red regions gradually contract, indicating a narrowing range of P^* that supports cluster cohesion. Elevated values of D_{R} impair cluster velocity coherence, potentially inducing cluster fission. Furthermore, distinct cohesion boundaries are typically observed for smaller α (e.g., $\alpha = 20°$, $60°$, $90°$), signifying an abrupt transition in Ψ at the transition point. Conversely, for larger α (e.g., $\alpha = 360°$), Ψ exhibits gradual variation with both P^* and D_{R}, suggesting that the internal properties of the clusters may vary with α. Intriguingly, at intermediate visual cone angles (e.g., $\alpha = 160°$, $180°$), as shown in Figs. 4(e) and 4(f), clusters are not cohesive at $P^* = 0$ and small D_{R}. However, cohesion emerges as D_{R} increases. This counterintuitive result, given the typically detrimental effect of D_{R} on cluster cohesion, can be explained by the larger angular rotations associated with larger D_{R} values. The increased rotational amplitude effectively expands agents' turning angles, thereby extending their perceptual range. This mechanism simultaneously enhances cluster stability and promotes global order formation. The phenomenon whereby moderate noise promotes global order or cohesion has also been observed in other SPP models.[37,38] Thus, the boundaries of cohesion reflect the interplay of competing factors.

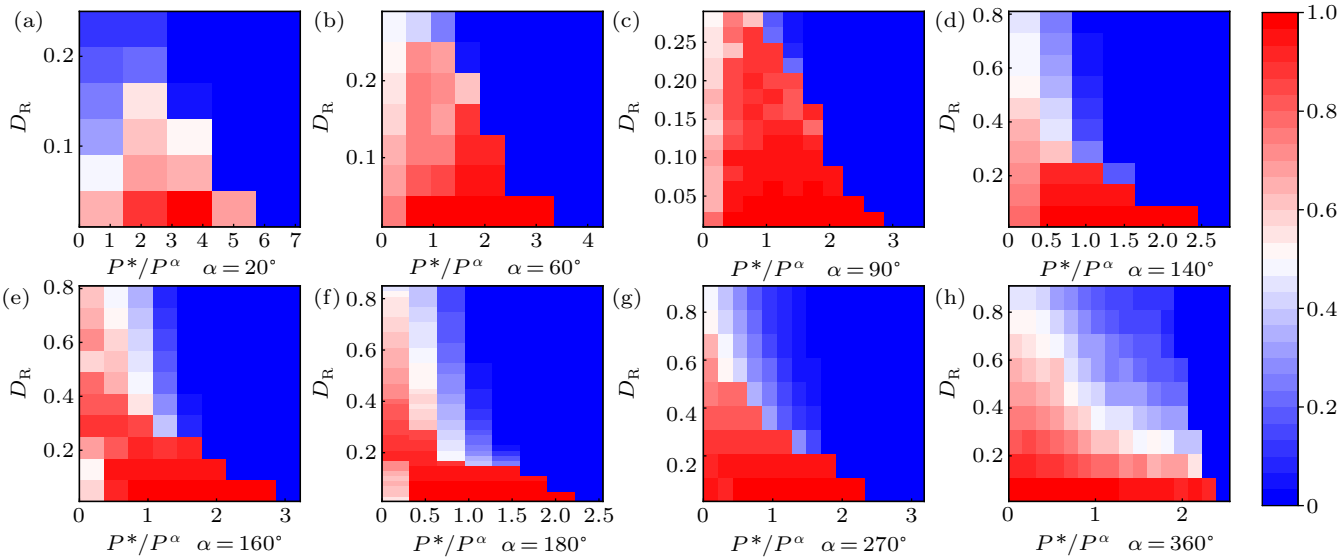


Fig. 4. Phase diagrams as a function of the rotational diffusion D_{R} and the ratio between the threshold and P^{α}, P^*/P^{α}. The calculations use $N_0 = 10000$ agents and different visual cone angles: $\alpha = 20°$ (a), $\alpha = 60°$ (b), $\alpha = 90°$ (c), $\alpha = 140°$ (d), $\alpha = 160°$ (e), $\alpha = 180°$ (f), $\alpha = 270°$ (g), $\alpha = 360°$ (h).

As shown in Fig. 3, cluster cohesion is significantly influenced by the threshold P^*. Once P^* exceeds a critical value, cohesion collapses. Since P^* is predetermined, cohesion fails to occur if this critical value is exceeded during parameter setting. Thus, investigation of the critical threshold has significant implications. Furthermore, the mechanisms governing the threshold that dictates cohesion are not immediately apparent. Our next task is to investigate the factors controlling the critical threshold, which we define as P_{g}. Clusters do not aggregate when $P^* > P_{\mathrm{g}} \times P^{\alpha}$. Simulations reveal a monotonic decrease in the critical threshold P_{g} with increasing α, as illustrated in Fig. 5(a). With a finite viewing radius R, larger values of α allow agents to interact with a larger number of neighboring agents within their field of view. However, the fact that the critical threshold is consistently higher than the local average density observed in Fig. 3 suggests that the un-

derlying mechanism is more complex than a simple density-dependent effect. Therefore, we first investigate the effects of density fluctuations within the visual cone region on cohesive boundary formation. To examine this relationship, we initially set the agents to a nonaligned state ($P^* = \infty$) to observe density fluctuations prior to cluster cohesion. Subsequently, we measured the density fluctuations within the detection area at $\alpha = 180^\circ$ for varying rotational diffusion coefficients ($D_R = 0.01, 0.1, 1$), as shown in Fig. 5(b). It can be seen that the density fluctuations are largely independent of D_R and exhibit a scaling consistent with that of an ideal gas, characterized by

$$\mu(N) = \frac{\lambda^N e^{-\lambda}}{N!}, \tag{4}$$

where μ represents the probability of observing N agents in a region with mean agent number $\lambda = A\rho$, A denotes the observation area, and ρ is the agent density. In our model, $\lambda = P^\alpha$. This behavior is expected, as our model excludes volume collisions, thus preventing the emergence of motility-induced phase separation (MIPS), which is commonly observed in active particle systems. Consequently, the density fluctuations in our model are expected to converge to the ideal gas limit in the long-time limit.

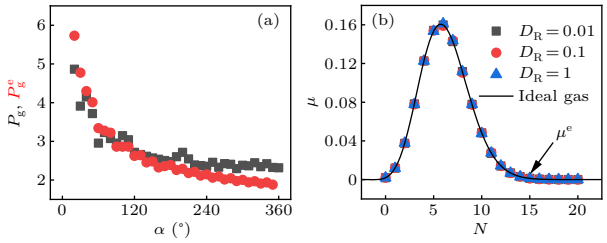


Fig. 5. Critical threshold and density fluctuation. (a) The critical thresholds for simulation P_g and theory P_g^e as a function of the visual cone α. (b) Local density probability distribution μ as a function of local agent number N, with $D_R = 0.01, 0.1, 1$, and with a visual cone of $\alpha = 180^\circ$. The black line represents the local density probability distribution of an ideal gas.

Substituting the critical agent count $N^e(\alpha = 180^\circ) = P_g(\alpha = 180^\circ) \times P^\alpha \approx 15$ corresponding to the visual cone $\alpha = 180^\circ$ into Eq. (4), we found the associated $\mu^e = 1.3 \times 10^{-3}$ resides in the tail region of the probability distribution μ, as shown in Fig. 5(b). While the area of the visual field Ω_i varies with different visual cones α, the local agent density distribution prior to cohesion remains consistent with the ideal gas model. Consequently, the functional form of $\mu(\alpha)$ is identical for different α (although with different λ values for different α). Therefore, we postulate that, for a fixed rotational diffusion D_R, the corresponding $\mu^e(\alpha)$ values for $P_g(\alpha)$ all lie in the tail of the μ function with approximately the same value. Given that $\alpha = 180^\circ$ represents an intermediate viewing angle, we select $\mu^e(\alpha) = \mu^e(\alpha = 180^\circ) = 1.3 \times 10^{-3}$. For each α, the μ^e determines the expected critical agent number $N^e(\alpha)$ through Eq. (4) and the expected critical threshold $P_g^e = N^e(\alpha)/P^\alpha$. The value of P_g^e is shown in Fig. 5(a). The predicted critical threshold P_g^e decreases monotonically with increasing α, following the same trend as the critical threshold P_g. This agreement validates our hypothesis that, for a fixed D_R, the critical threshold P_g at different values of α corresponds to an identical μ^e. This finding suggests that the critical threshold is partly determined by density fluctuations. Let us summarize the microscopic mechanisms underlying cluster formation. At the start of the simulations, before any cohesion occurs, the number of agents, k_i, within the field of view of agent i fluctuates according to Eq. (4). When the count k_i exceeds the threshold P^*, agent i transitions to an aligned state ($P_i = 1$). The stability of this alignment is strongly influenced by D_R. Specifically, for small values of D_R, the alignment persists, facilitating the formation of stable clusters. Conversely, for large D_R, agents exhibit frequent reorientation, resulting in the loss of alignment ($P_i = 0$) and subsequent cluster disassembly.

With a clearer understanding of the mechanisms influencing the cohesion boundaries, we now shift our focus to the internal structure of the resulting clusters. Notably, the cluster shape is sensitive to the visual cone α, changing from a linear (chain-like) configuration to a disk-like structure as α increases, as shown in Fig. 2. A particularly interesting observation is that for small α, agents at the front of the cluster often exhibit misalignment ($P_i = 0$), whereas for large α, almost all agents inside the cluster are in an aligned state ($P_i = 1$). To quantify the degree of agent alignment within clusters, we define the alignment fraction as $\Phi = n(P_i = 1)/n_c$, where $n(P_i = 1)$ is the number of aligned agents and n_c is the total number of agents in the clusters. The dependence of Φ on α is illustrated in Fig. 6(a). For $\alpha < 180^\circ$, the alignment fraction is relatively low, around 0.1, with a minimum observed near $\alpha = 90^\circ$. In contrast, a significant jump in Φ is seen near $\alpha = 180^\circ$, reaching a value of 0.9. Moreover, we calculated the cluster density ρ as a function of α, as shown in Fig. 6(b), finding a nonmonotonic relationship with a maximum density around $\alpha = 90^\circ$.

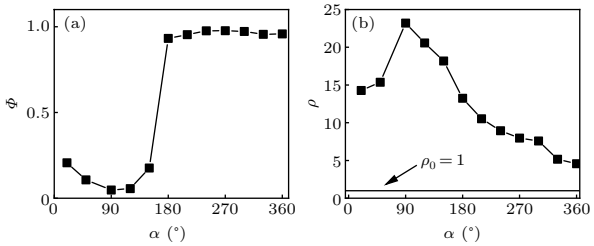


Fig. 6. Proportion of aligned agents and cluster cohesion. (a) Proportion Φ of aligned agents as a function of the visual cone α. (b) The density ρ of the cluster as a function of the visual cone α. The initial density is $\rho_0 = 1$.

This behavior aligns with the 'chasing effect' described in Ref. [32]. For $\alpha < 180^\circ$, leading-edge agents lack neighbors within their field of view, promoting a misaligned state

($P_i = 0$) and reducing the alignment fraction Φ. The rotational diffusion D_R further disrupts the ballistic motion of these misaligned agents, causing trailing agents to close the gap. This leads to spatial compaction and an increase in cluster density ρ. The interplay between low Φ and high ρ is most pronounced at $\alpha = 90°$, where Φ reaches its minimum and ρ its maximum. Conversely, for $\alpha > 180°$, leading-edge agents can perceive their neighbors, favoring alignment ($P_i = 1$). This alignment reduces the chasing effect, resulting in a decrease in cluster density ρ. Thus, ρ monotonically decreases with increasing α for $\alpha > 180°$. Furthermore, a higher threshold P^* increases the proportion of misaligned agents within the cluster, which enhances the chasing effect and leads to a higher cluster density ρ. This explains the observed monotonic increase in ρ with P^*, as shown in Fig. 3(a). Similarly, as α increases, the chasing effect weakens, causing the cluster to expand spatially along the direction of collective motion. This results in a morphological transition from a linear to a disk-like geometry, as demonstrated in Fig. 2.

4. Conclusions and outlook

In this article, we have shown that the self-assembly of active agents into compact, velocity-polarized clusters can be achieved through the joint regulation of agent motion by visual perception and threshold. It can be seen that by selecting an appropriate threshold, spatial condensation and concordant motion emerge concurrently within a certain range of viewing angles. The effects of density fluctuations and noise on the cohesion boundaries and critical threshold were investigated. The chasing mechanism was applied to explain the cohesion and density variations of clusters.

The agent arrangement achieved in our model satisfies key requirements for robotic deployments, demonstrating both robustness and scalability. Specifically, the self-organizing behavior of the group remains stable under perturbations, including kinetic noise and the addition or removal of individual agents. While similar behaviors have been reported in the literature,[39–42] the integration of these features within a single framework is nontrivial. We attribute this emergent behavior to the heterogeneous kinetic properties of the agents.

Our model offers a potential framework for generating directed collective behavior in robotic/UAV systems, as each agent simply adjusts its motion based on its own perception, without the need for controlling interactions with multiple neighbors. High-density stable formations enable efficient and reliable interagent communication and perception,[43,44] while also reducing detectability in complex terrains and electromagnetic environments. However, increased density raises the risk of collisions, which necessitates careful design considerations. Our studies provide clues about the connection between the perception rule and density, potentially informing the design of robot/UAV swarms. A strategy for precluding collisions among robots/UAVs centers on providing agents with vision sensors or radar systems that monitor the locations and spatial separations of other nearby agents. When the distance separating agents decreases below a predefined safety parameter, the agent modifies its speed to prevent a collision from occurring.[45–47] The comprehensive consideration of collisions in collective motion systems is a topic for exploration in future studies.

Acknowledgments

Project supported by the Postgraduate Research & Practice Innovation Program of Jiangsu Province (Grant No. KYCX24_0139). R. C. was funded by the Youth Independent Innovation Fund of PLA Army Engineering University (Grant No. KYJBJKQTZQ23006).

References

[1] Cavagna A, Cimarelli A, Giardina I, Parisi G, Santagati R, Stefanini F and Viale M 2010 *Proc. Natl. Acad. Sci. USA* **107** 11865
[2] Huth A and Wissel C 1994 *Ecol. Model.* **75–76** 135
[3] Czirók A, Ben-Jacob E, Cohen I and Vicsek T 1996 *Phys. Rev. E* **54** 1791
[4] Silverberg J L, Bierbaum M, Sethna J P and Cohen I 2013 *Phys. Rev. Lett.* **110** 228701
[5] Elgeti J, Winkler R G and Gompper G 2015 *Rep. Prog. Phys.* **78** 056601
[6] Rubenstein M, Cornejo A and Nagpal R 2014 *Science* **345** 795
[7] Lavergne F A, Wendehenne H, Bäuerle T and Bechinger C 2019 *Science* **364** 70
[8] Turgut A E, Çelikkanat H, Gökçe F and Şahin E 2008 *Swarm Intell.* **2** 97
[9] Yigit B, Alapan Y and Sitti M 2020 *Soft Matter* **16** 1996
[10] Daingade S and Sinha A 2016 *Int. J. Micro Air Veh.* **8** 240
[11] Wu J, Yu Y, Ma J, Wu J, Han G, Shi J and Gao L 2021 *IEEE Trans. Veh. Technol.* **70** 12477
[12] Wu Q, Zeng Y and Zhang R 2018 *IEEE Trans. Wirel. Commun.* **17** 2109
[13] Vicsek T, Czirók A, Ben-Jacob E, Cohen I and Shochet O 1995 *Phys. Rev. Lett.* **75** 1226
[14] Chepizhko O, Altmann E G and Peruani F 2013 *Phys. Rev. Lett.* **110** 238101
[15] Copenhagen K, Quint D A and Gopinathan A 2016 *Sci. Rep.* **6** 31808
[16] Yllanes D, Leoni M and Marchetti M C 2017 *New J. Phys.* **19** 103026
[17] Chatterjee S, Mangeat M, Woo C U, Rieger H and Noh J D 2023 *Phys. Rev. E* **107** 024607
[18] Chepizhko O and Peruani F 2013 *Phys. Rev. Lett.* **111** 160604
[19] Gómez-Nava L, Bon R and Peruani F 2022 *Nat. Phys.* **18** 1494
[20] Kunal B and Tamás V 2014 *J. R. Soc. Interface* **11** 20140674
[21] Qi J, Bai L, Xiao Y, Wu W and Liu L 2020 *IEEE Access* **8** 160490
[22] Lan X, Xu W, Zhao Z and Liu G 2021 *IEEE-CAA J. Autom. Sin.* **8** 648
[23] Ginelli F, Peruani F, Pillot M H, Chaté H, Théraulaz G and Bon R 2015 *Proc. Natl. Acad. Sci. USA* **112** 12729
[24] Liu C, Fu X, Liu L, Ren X, Chau C K, Li S, Xiang L, Zeng H, Chen G, Tang L H, Lenz P, Cui X, Huang W, Hwa T and Huang J D 2011 *Science* **334** 238
[25] Farrell F D C, Marchetti M C, Marenduzzo D and Tailleur J 2012 *Phys. Rev. Lett.* **108** 248101
[26] Tailleur J and Cates M E 2008 *Phys. Rev. Lett.* **100** 218103
[27] Bhattacharya K and Chakraborty A 2022 *Phys. Rev. E* **105** 044124
[28] Li W and Wang X 2007 *Phys. Rev. E* **75** 021917
[29] Moussaïd M, Helbing D and Theraulaz G 2011 *Proc. Natl. Acad. Sci. USA* **108** 6884
[30] Gibson J J 2009 *Br. J. Psychol.* **100** 259
[31] McComb D M and Kajiura S M 2008 *J. Exp. Biol.* **211** 482

[32] Meng F, Feng C, Ma W, Cheng R, Wang J and Wang W 2024 *Phys. Lett. A* **495** 129307
[33] Zhou Y, Li Y and Marchesoni F 2023 *Chin. Phys. Lett.* **40** 100505
[34] Costanzo A and Hemelrijk C K 2018 *J. Phys. D: Appl. Phys.* **51** 134004
[35] Barberis L and Peruani F 2016 *Phys. Rev. Lett.* **117** 248001
[36] Jusup M, Holme P, Kanazawa K, Takayasu M, Romić I, Wang Z, Geček S, Lipić T, Podobnik B, Wang L, Luo W, Klanjšček T, Fan J, Boccaletti S and Perc M 2022 *Phys. Rep.* **948** 1
[37] Aung E, McClure J E and Abaid N 2024 2024 *Phys. Rev. E* **110** L062102
[38] Durve M, Saha A and Sayeed A 2018 *Eur. Phys. J. E* **41** 49
[39] Martin D, Chaté H, Nardini C, Solon A, Tailleur J and Van Wijland F 2021 *Phys. Rev. Lett.* **126** 148001
[40] Chen G 2016 *IEEE Trans. Autom. Control* **62** 636
[41] Slavkov I, Carrillo-Zapata D, Carranza N, Diego X, Jansson F, Kaandorp J, Hauert S and Sharpe J 2018 *Sci. Robot.* **3** eaau9178
[42] Bekmezci I, Sahingoz O K and Temel S 2013 *Ad Hoc Netw.* **11** 1254
[43] Wu J, Zou L, Zhao L, Al-Dubai A, Mackenzie L and Min G 2019 *Comput. Netw.* **158** 132
[44] Liu W and Gao Z 2020 *Comput. Commun.* **153** 95
[45] Li Y, Du W, Yang P, Wu T, Zhang J, Wu D and Perc M 2019 *IEEE Internet Things J.* **6** 1866
[46] Roelofsen S, Gillet D and Martinoli A 2015 2015 *IEEE/RSJ International Conference on Intelligent Robots and Systems (IROS)* pp. 4810-4817
[47] Luo C, McClean S I, Parr G, Teacy L and De Nardi R 2013 *IEEE Trans. Veh. Technol.* **62** 2749